

# Feature Space Analysis by Guided Diffusion Model

Kimiaki Shirahama *IEEE*, Miki Yanobu, Kaduki Yamashita, Miho Ohsaki *IEEE Senior*

**Abstract**—One of the key issues in Deep Neural Networks (DNNs) is the black-box nature of their internal feature extraction process. Targeting vision-related domains, this paper focuses on analysing the feature space of a DNN by proposing a *decoder* that can generate images whose features are guaranteed to closely match a user-specified feature. Owing to this guarantee that is missed in past studies, our decoder allows us to evidence which of various attributes in an image are encoded into a feature by the DNN, by generating images whose features are in proximity to that feature. Our decoder is implemented as a *guided diffusion model* that guides the reverse image generation of a pre-trained diffusion model to minimise the Euclidean distance between the feature of a clean image estimated at each step and the user-specified feature. One practical advantage of our decoder is that it can analyse feature spaces of different DNNs with no additional training and run on a single COTS GPU. The experimental results targeting CLIP’s image encoder, ResNet-50 and vision transformer demonstrate that images generated by our decoder have features remarkably similar to the user-specified ones and reveal valuable insights into these DNNs’ feature spaces.

**Index Terms**—Feature space, Diffusion model, Guidance, Multimodal embedding space.

## I. INTRODUCTION

DEEP learning is often referred to as representation learning or feature learning that extracts useful features (data representations) through statistical analysis on a large amount of data [1], [2]. In vision-related domains, this is typically demonstrated by impressive image classification performances achieved through an output layer that performs simple linear classification on top of extracted features [3], [4]. In addition, regardless of whether a deep neural network (DNN) is pre-trained or not, features extracted by it can be used as a source to carry out various tasks. For example, cross-modal retrieval is implemented via similarity search on features (embeddings) extracted by encoders trained on different modalities [5], [6], image/video captioning is performed by passing features extracted by an encoder to a decoder [7], and image editing is done using features extracted from some inputs (e.g., image, text prompt, sketch, etc.) as conditions [8], [9].

Despite the above-mentioned extensive exploration of utilising features extracted by DNNs, very limited attention has been given to understanding those features. In addition, it is now known that overparameterised DNNs, which memorise atypical examples and outliers/mislabelled examples, offer an improved generalisation power rather than overfitting [10], [11]. This motivates us to investigate what kind of feature

space is built by such a DNN. Also, visual-semantic embeddings are learned so that an image and its relevant text caption are encoded into close points (i.e., embeddings) in a common feature space, but they are not the same [5], [6]. This evokes our interest in what kind of image (or caption) is characterised by an embedding located between those of the relevant image and caption.

To analyse the feature space of a DNN, this paper addresses the development of a *decoder* that generates an image whose feature closely matches a user-specified one. This decoder allows us to visually reveal which of various attributes in an image are encoded into a feature extracted by the DNN, by generating images whose features are in proximity to this feature. Furthermore, it could be possible to generate, for example, a “hard negative” image whose feature is difficult to distinguish from the one extracted from a semantically dissimilar image [5], a “rare” image whose feature lies far from the feature of every image in a dataset, and a “memorised” image for which a small perturbation of its feature leads to a different prediction [12]. Therefore, the decoder developed in this paper opens up many possibilities for analysing and improving the feature space of the DNN (mining the above-mentioned images is our future work).

Although some decoders have been developed in similar contexts [13]–[15], they have the following two problems (please see the next section for more details): First, these decoders do not ensure that the feature of a generated image is close to a user-specified one. In other words, they have no control on the correspondence between a generated image and its feature. Second, training decoders in [13]–[15] requires large-scale computational resources that are unavailable for ordinary researchers.

To overcome these problems, we focus on a diffusion model that is a probabilistic generative model to generate images by progressively denoising pure Gaussian noise, because of its proven capability to generate high-quality images [16], [17]. In particular, our decoder is implemented as a *guided diffusion model* where a diffusion model is used as a generic image generator and its image generation is guided to generate images that minimise or lower a loss function [18]–[27]. The guidance of our decoder is based on a loss function that measures the Euclidean distance between a user-specified feature and the one of a generated image. Our decoder solves the two problems described above. The first problem is handled by the loss function enforcing that the feature of a generated image closely matches a specified one. In addition, our decoder bypasses the second problem because it does not require to train a diffusion model, but just uses a pre-trained diffusion model while computing a gradient of the loss function. Actually, our decoder can run on a single COTS GPU

0000–0000/00\$00.00/© 2021 IEEE has more than 16GB of VRAM.

K. Shirahama, M. Yanobu, K. Yamashita and M. Ohsaki are with Department of Information Systems Design, Doshisha University, Japan.

This work has been initiated from M. Yanobu’s bachelor thesis at Department of Information Systems Design, Doshisha University, Japan.

In summary, four key contributions of this paper are as follows:

- 1) Our decoder generates images whose features are ensured to closely match user-specified ones, which enables us to perform rigorous analysis of a DNN's feature space based on the short Euclidean distances between those features. To our best knowledge, we are the first to propose this kind of rigorous feature space analysis. In particular, the experiments targeting CLIP's image encoder, ResNet-50 and Vision Transformer (ViT) reveal valuable insights into their feature spaces, such as little sensitivity of CLIP's image encoder to an object's anatomical structure, loss of detailed information by legacy ResNet-50, ViT's excessive focus on the main object in an image, and weak image-text association in CLIP's feature space.
- 2) Our decoder is general and training-free. By general, it can be used to analyse the feature space of any DNN that encodes an image into a feature. By training-free, our decoder needs no additional training, that is, its feature space analysis can be performed as long as one implements a feature extraction process by a DNN.
- 3) Compared to existing guided diffusion models [18]–[27], this paper introduces a new guidance that uses the Euclidean distance between image features as a loss function. Especially, by borrowing the idea in [26], [27], a noisy image generated at each step of the reverse process is used to predict a clean image from which a feature is extracted and compared against a user-specified one. This eliminates the need for specialized handling of the noisy image.
- 4) Some techniques like early step emphasis for self-recurrence and gradient normalisation and clipping are devised to improve our decoder's image generation.

Finally, the codes and data used in this paper as well as high-resolution figures showing generated images are available on our github repository <https://github.com/KimiakiShirahama/FeatureSpaceAnalysisByGuidedDiffusionModel>.

## II. RELATED WORK

This section provides a survey of existing studies related to this paper from the perspective of guided diffusion models and the one of decoders.

Many guidance approaches have been developed to provide different controls over the image generation of a diffusion model in order to devise various applications such as text-to-image [18]–[20], [22], [24]–[27], image inpainting [20], [26], [27], object/style/layout manipulation [21], [23], [26], [27], composition between images [23] and image segmentation [21]. Regarding loss functions used in existing guided diffusion models, the most basic ones like classifier guidance [18], classifier-free guidance [19] and CLIP guidance [20] measure a probability or score indicating how relevant a text prompt is to a noisy image generated at each step. These loss functions are then extended to examine whether each of subject tokens in a prompt is attended to by some patches in a generated image [22], whether a generated image satisfies

propositional statements deduced from a prompt [25] and whether a generated image has a plausible depth map [24]. In addition, various loss functions are proposed to assess different aspects such as an object's position, size, shape and appearance [23], an object's pose and position, personal identity and painting style [26], [27] and the distribution of colors and the one of labels in a generated segmentation image [21].

To our best knowledge, no guided diffusion model has been proposed to generate an image whose feature is very close to a user-specified one as ours does. Our method is inspired by [26], [27] that demonstrates the effectiveness of applying a loss function to a clean image, which is analytically predicted from the noisy image generated at each step of the reverse process. In other words, such clean images are naturally imperfect but still useful for providing appropriate guidance to minimise the loss function. By borrowing this idea, we propose a guided diffusion model that employs a loss function designed to compute the Euclidean distance between a user-specified feature and the one extracted from a clean image predicted at each reverse step.

To analyse the feature space of a DNN, some researchers have investigated decoders that invert a feature back into an image from which this feature is likely to be extracted. Teterwak *et al.* adopts the framework of conditional GAN to train a decoder (generator) in which the operation of batch normalisation is modulated based on a given feature (to be precise logit vector) [13]. Ramesh *et al.* construct a decoder as a diffusion model that generates an image by combining a given feature with the embedding of each step and also deriving four extra textual tokens of context from it [14]. Bordes *et al.* build a decoder as a diffusion model by developing conditional batch normalisation layers that take a given feature as conditioning [15]. As inferred from the above-mentioned studies, in principle, one can devise a decoder as any conditional generative model that generates an image, which is likely to be encoded into a user-specified feature.

However, this approach involves two crucial problems: First, just using a user-specified feature as conditioning lacks checking how close the feature of a generated image is to it. The experiment in Section IV-B shows that although images generated by a conditional diffusion model in [15] are plausible, their features are distant from the corresponding specified features. Second, training generative models on large-scale datasets requires very expensive computational costs. In particular, a diffusion model should be employed as a decoder because of its capability to generate high-quality images, but training it is prohibitively expensive. For instance, training the diffusion model in [18] consumes 150-1000 V100 GPU days to produce high-quality images [28]. Moreover, training stable diffusion [17] demands over 24 days on 256 A100 GPUs [29]. Therefore, it is infeasible for ordinary researchers to train a diffusion-model decoder on a large-scale dataset. Therefore, we employ a guided diffusion model that is based on a pre-trained diffusion model and needs no additional training.

Finally, researchers in the field of NLP have recently begun investigating decoders that invert a text sentence from its feature (embedding) encoded by an LLM, due to the privacy

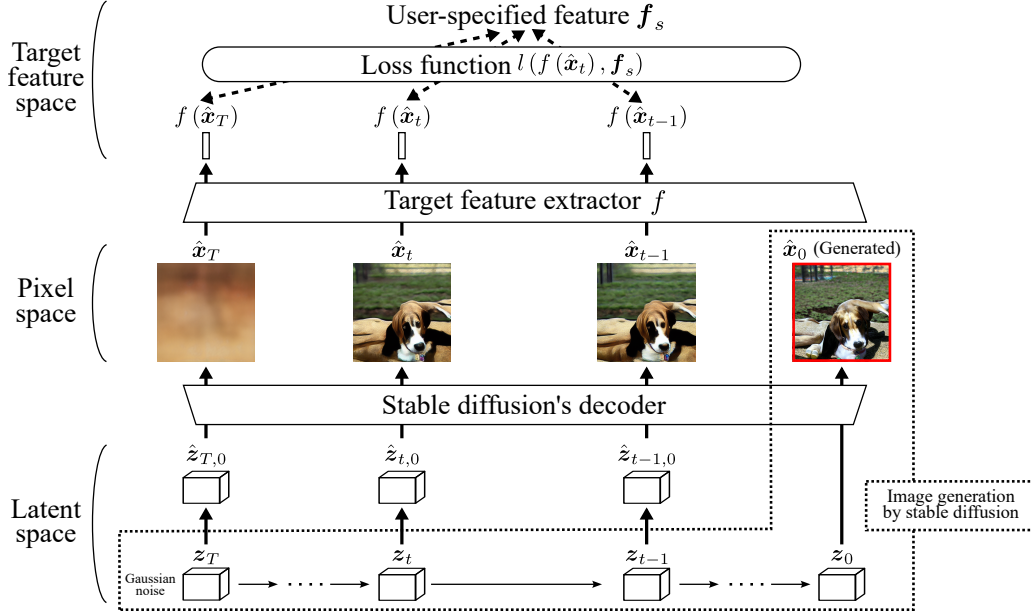


Fig. 1. An overview of our decoder based on a guided diffusion model. Here, stable diffusion’s image generation is guided to generate an image whose feature closely matches a user-specified one  $f_s$  by estimating a clean latent representation  $\hat{z}_{t,0}$  from  $z_t$  at step  $t$ , generating the corresponding image  $\hat{x}_t$  from  $\hat{z}_{t,0}$ , extracting the feature  $f(\hat{x}_t)$  of  $\hat{x}_t$ , and computing the loss as the squared Euclidean distance between  $f(\hat{x}_t)$  and  $f_s$ .

concern that third-party services might reproduce the original text from its feature [30], [31]. Our long-term goal is to combine such a text decoder with the image decoder in this paper in order to analyse a multimodal feature space.

### III. OUR GUIDED-DIFFUSION-MODEL-BASED DECODER FOR FEATURE SPACE ANALYSIS

This section firstly provides an overview of our decoder’s image generation and then presents its algorithmic procedure as well as implementation details.

#### A. Overview of Our Decoder

Fig. 1 shows an overview of our decoder consisting of the following three main components: The first is a pre-trained diffusion model, especially stable diffusion [17] illustrated by the dotted region in Fig. 1, that establishes the foundational image generation process of our decoder. The second component depicted by the trapezium is the target feature extractor  $f$  whose feature space is our analysis target. That is, a guidance signal for controlling stable diffusion’s image generation is computed in  $f$ ’s feature space via the loss function  $l(f(\hat{x}_t), f_s)$ , which is the last component expressed by the rectangle with rounded corners. Taking into account the relation of these three main components, more details of our decoder is explained below.

Our decoder is an extension of the guided diffusion model proposed in [26], [27]. As depicted by the dotted region, stable diffusion [17]<sup>1</sup> is used as a backbone diffusion model while it is clearly possible to use any other diffusion model. In stable diffusion, the reverse process is performed in the latent

space built by a pre-trained autoencoder in order to attain perceptually equivalent but computationally efficient image generation. Specifically, a latent representation  $z_T$  (in our case feature map of shape  $4 \times 64 \times 64$ ) defined by pure Gaussian noise is progressively denoised into its clean version  $z_0$ , from which the image  $\hat{x}_0$  is generated through the decoder.

Our guidance modulates each reverse step to sample  $\hat{z}_{t-1}$  from  $\hat{z}_t$  ( $1 \leq t \leq T$ ). The core idea is that a clean latent representation  $\hat{z}_{t,0}$  which is imperfect but still useful can be estimated as follows [26], [27]:

$$\hat{z}_{t,0} = \frac{z_t - \sqrt{1 - \bar{\alpha}_t} \epsilon_\theta(z_t, t)}{\sqrt{\bar{\alpha}_t}}. \quad (1)$$

This equation is derived based on the forward process to create  $z_t = \sqrt{\bar{\alpha}_t} z_0 + \sqrt{1 - \bar{\alpha}_t} \epsilon$  where  $\epsilon \sim \mathcal{N}(\mathbf{0}, \mathbf{I})$  is source noise and  $\bar{\alpha}_t = \prod_{i=1}^t \alpha_i = \prod_{i=1}^t (1 - \beta_i)$  and  $1 - \bar{\alpha}_t$  respectively indicate the scale of clean  $z_0$  and that of  $\epsilon$  according to the pre-defined variance schedule  $\beta_1, \dots, \beta_t$ . In Eq. (1),  $z_0$  is approximated as  $\hat{z}_{t,0}$  using  $\epsilon_\theta(z_t, t)$  that is source noise predicted by passing  $z_t$  and  $t$  to stable diffusion’s UNet parameterised by  $\theta$ <sup>2</sup>.

As illustrated in Fig. 1, the image  $\hat{x}_t$  is then generated by feeding  $\hat{z}_{t,0}$  into stable diffusion’s decoder. Thereby, according to the target feature extractor  $f$ , it is possible to examine how close the feature  $f(\hat{x}_t)$  of  $\hat{x}_t$  is to a user-specified feature  $f_s$  in terms of their squared Euclidean distance below:

$$l(f(\hat{x}_t), f_s) = \|f(\hat{x}_t) - f_s\|_2^2. \quad (2)$$

Our guidance uses  $l(f(\hat{x}_t), f_s)$  as a loss function to sample  $z_{t-1}$  that is likely to serve as the source for generating  $\hat{z}_{t-1,0}$ , followed by the image  $\hat{x}_{t-1}$  whose feature  $f(\hat{x}_{t-1})$  is closer

<sup>1</sup>The exact checkpoint name is sd-v1-4.ckpt available on <https://huggingface.co/CompVis/stable-diffusion-v-1-4-original>.

<sup>2</sup>Following [26], [27], an empty string is also passed to implement unconditional image generation using text-conditional stable diffusion.

to  $f_s$  than  $f(\hat{x}_t)$ . Specifically, the predicted source noise  $\epsilon_\theta(z_t, t)$  for  $\hat{z}_t$  is modified by the gradient of  $l(f(\hat{x}_t), f_s)$  in terms of  $z_t$ :

$$\epsilon'_\theta(z_t, t) = \epsilon_\theta(z_t, t) - w_g \nabla_{z_t} l(f(\hat{x}_t), f_s), \quad (3)$$

where  $w_g$  is a hyper-parameter to balance it with  $\epsilon_\theta(z_t, t)$ . Finally,  $z_{t-1}$  is sampled by the following standard sampling procedure [16] except that  $\epsilon_\theta(z_t, t)$  is replaced with  $\epsilon'_\theta(z_t, t)$ <sup>3</sup>:

$$z_{t-1} = \frac{1}{\sqrt{\alpha_t}} \left( z_t - \frac{1 - \alpha_t}{\sqrt{1 - \alpha_t}} \epsilon'_\theta(z_t, t) \right) + \sqrt{\beta_t} \Delta, \quad (4)$$

where  $\Delta$  is noise sampled from  $\mathcal{N}(\mathbf{0}, \mathbf{I})$ . By repeating the above-mentioned sampling of  $z_{t-1}$  from  $z_t$ , our guided diffusion model generates an image  $\hat{x}_0$  whose feature  $f(\hat{x}_t)$  minimises the squared Euclidean distance to  $f_s$ .

## B. Details of Our Decoder

**Algorithm 1** Image generation guided to generate an image whose feature closely matches a user-specified one

**Require:** Target feature extractor  $f$ , stable diffusion’s UNet  $\epsilon_\theta$  and decoder, number of reverse steps  $T$ , variance schedule  $\{\beta_1, \dots, \beta_T\}$ , user-specified feature  $f_s$ , gradient weight  $w_g$

```

1: Sample  $z_T$  from  $\mathcal{N}(\mathbf{0}, \mathbf{I})$ 
2: for  $t = T, \dots, 1$  do
3:   Set the number of self-recurrence iterations  $K$  based on
   the early step emphasis
4:   for  $k = 1, \dots, K$  do
5:     Compute  $\hat{z}_{t,0}$  using Eq. (1)
6:     Generate  $\hat{x}_t$  from  $\hat{z}_{t,0}$  via the virtual image save
7:     Compute the feature  $f(\hat{x}_t)$  of  $\hat{x}_t$ 
8:     Compute  $l(f(\hat{x}_t), f_s)$  using Eq. (2) and its gradient
      $\nabla_{z_t} l(f(\hat{x}_t), f_s)$ 
9:     Normalise and clip  $\nabla_{z_t} l(f(\hat{x}_t), f_s)$ 
10:    Compute  $\epsilon'_\theta(z_t, t)$  using Eq. (3)
11:    Sample  $z_{t-1}$  using Eq. (4)
12:    if  $k < K$  then
13:      Resample  $z_t$  from  $z_{t-1}$  using Eq. (5)
14:    end if
15:  end for
16: end for
17: Generate  $\hat{x}_0$  from  $z_0$  by stable diffusion’s decoder
18: return  $\hat{x}_0$ 
```

Algorithm 1 shows a flow of operations in our decoder<sup>4</sup>. The main operations at lines 1, 5-8, 10, 11 and 17 have been already described in the previous subsection. The following

<sup>3</sup>Our decoder is devised by forking the implementation provided by [26], [27] where  $z_{t-1}$  is deterministically computed using  $\hat{z}_{t,0}$  and  $\epsilon'_\theta(z_t, t)$ . We changed this  $z_{t-1}$  computation to the standard  $z_{t-1}$  sampling in Eq. 4, which significantly improved the quality of generated images.

<sup>4</sup>Although our decoder is based on the guided diffusion model proposed in [26], [27], preliminary experiments let us exclude one of its main modules, called backward universal guidance. The reason is that this module directly optimises pixels in an image without considering the progress of the reverse process, which actually offers little reduction of the loss function and often produces very unrealistic or corrupted images.

part details the other operations such as early step emphasis at line 3, self-recurrence at lines 4, 12 and 13, virtual image save at line 6, and gradient normalisation and clipping at line 9.

Self-recurrence is motivated by the fact that  $T$  reverse steps ( $T = 1000$  in our case) are insufficient to generate an image whose feature is within acceptable proximity to  $f_s$ . With respect to this, increasing  $T$  is difficult because the diffusion model in our decoder is pre-trained with this  $T$ . To overcome this, self-recurrence [26], [27], [32], [33] is employed to resample  $z_t$  from  $z_{t-1}$  by following the standard forward step below:

$$z_t = \sqrt{\alpha_t} z_{t-1} + \sqrt{1 - \alpha_t} \Delta \quad \text{where } \Delta \sim \mathcal{N}(\mathbf{0}, \mathbf{I}). \quad (5)$$

Since this resampled  $z_t$  preserves the information in  $z_{t-1}$ , it is likely to yield an image whose feature is closer to  $f_s$  than  $z_t$  before self-recurrence. This way, self-recurrence iteratively refines  $z_t$  by incorporating the information from the subsequent  $(t - 1)$ th step while maintaining the noise scale at the current  $t$ th step.

The overall object layout of a generated image is primarily established during early reverse steps [16]. Thus, our decoder’s image generation fails if this layout is inadequate. To address this, we design an early step emphasis strategy that prioritises early reverse steps. Specifically, for the first  $T'$  reverse steps (i.e.,  $t \geq T - T'$  in Algorithm 1) the number of self-recurrence iterations  $K$  is set to a large value while using a much smaller  $K$  at the remaining steps. In our case,  $K$  is set to 1000 and 8 at the first  $T' = 5$  reverse steps and the others, respectively. Appendix C provides an ablation study to empirically show the effectiveness of the early step emphasis strategy.

Stable diffusion’s decoder produces an image  $\hat{x}_t$  as a tensor of shape  $C \times H \times W$  (in our case  $C = 3$  and  $H = W = 512$ ) where pixels can take both negative and positive values. The ideal way to precisely compute  $\nabla_{z_t} l(f(\hat{x}_t), f_s)$  is to scale values in  $\hat{x}_t$  and save  $\hat{x}_t$  into an actual image file, which is then loaded and encoded into  $f(\hat{x}_t)$  through  $f$ . However, this is infeasible because the computation graph is broken when  $\hat{x}_t$  is saved into an external image file. Thus, to simulate image save on a GPU’s VRAM, a virtual image save module is implemented so that  $\hat{x}_t$  is scaled and rounded to make pixels take discrete values between 0 and 255<sup>5</sup>. Here, straight through estimator [34] is used to approximate the backpropagation over the round function of  $\hat{x}_t$  as its identify function.

One crucial issue to stabilise our decoder’s image generation is how to balance  $\epsilon_\theta(z_t, t)$  and  $\nabla_{z_t} l(f(\hat{x}_t), f_s)$  to compute  $\epsilon'_\theta(z_t, t)$  in Eq. (3). Another key issue is that exceptionally large values in  $\nabla_{z_t} l(f(\hat{x}_t), f_s)$  excessively distort the originally predicted values in  $\epsilon_\theta(z_t, t)$ , leading to the generation of corrupted images. For the first issue,  $\nabla_{z_t} l(f(\hat{x}_t), f_s)$  is normalised by multiplying  $\frac{\|\epsilon_\theta(z_t, t)\|_2}{\|\nabla_{z_t} l(f(\hat{x}_t), f_s)\|_2}$  where  $\|a\|_2$  is the L2 norm computed by flattening the tensor  $a$  into a vector.

<sup>5</sup>Due to the small difference in image rescaling,  $f(\hat{x}_t)$  obtained via the visual image save differs marginally from  $f(\hat{x}_t)$  obtained by loading an actual image file. In the case where  $f$  is defined as CLIP’s image encoder to produce 1024-dimensional feature vectors, their squared Euclidean distance is about 0.011, resulting in only minor semantic variations in generated images.

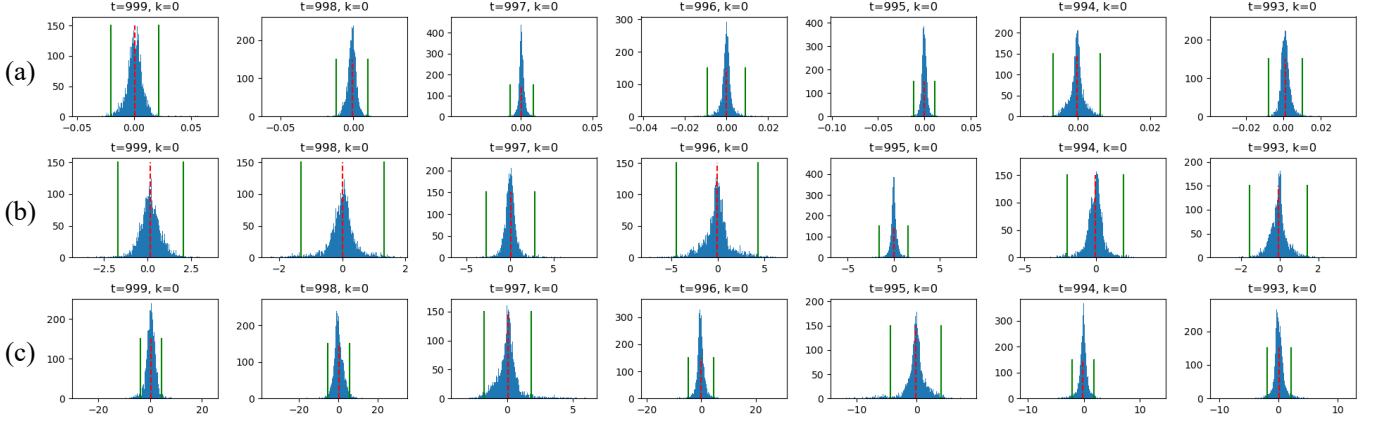


Fig. 2. Distributions of values in  $\nabla_{z_t} l(f(\hat{x}_t), \mathbf{f}_s)$  obtained at the first self-recurrence (i.e.,  $k = 0$ ) iteration of the first seven reverse steps (i.e.,  $t = 999$ -993th steps) when the target feature extractor  $f$  is defined as CLIP's image encoder (a), ResNet-50 (b) and ViT-H/14 (c). Here,  $\mathbf{f}_s$  is specified as the feature extracted from the top-left actual image in Fig. 3 (please see Section IV for more details). In each visualised distribution, the dotted indicates the mean and the solid lines represent three times standard deviation for (a) and (b) and twice standard deviation for (c).

The normalised  $\nabla_{z_t} l(f(\hat{x}_t), \mathbf{f}_s)$  has the same contribution as  $\epsilon_\theta(z_t, t)$  in terms of their L2 norms. For the second issue, we found that values in  $\nabla_{z_t} l(f(\hat{x}_t), \mathbf{f}_s)$  approximately follow a Gaussian distribution whose mean is nearly zero as demonstrated in Fig. 2. Based on this, gradient clipping is designed such that if values in  $\nabla_{z_t} l(f(\hat{x}_t), \mathbf{f}_s)$  fall outside the range  $\pm \nabla_{thres}$ , they are clipped to their nearest boundary, either  $\nabla_{thres}$  or  $-\nabla_{thres}$ .

In particular, as depicted by solid lines in Fig. 2,  $\nabla_{thres}$  is set to three times the standard deviation of values in  $\nabla_{z_t} l(f(\hat{x}_t), \mathbf{f}_s)$  when  $f$  is CLIP's image encoder or ResNet-50. When using ViT-H/14 as  $f$ ,  $\nabla_{thres}$  is set to twice the standard deviation due to the broad spread of values in  $\nabla_{z_t} l(f(\hat{x}_t), \mathbf{f}_s)$  as shown in Fig. 2 (c). Finally,  $\nabla_{z_t} l(f(\hat{x}_t), \mathbf{f}_s)$  fixed by the above-mentioned gradient normalisation and clipping is weighted by  $w_g$  to compute  $\epsilon'_\theta(z_t, t)$  in Eq. (3). All the experiments in the next section are done by fixing  $w_g$  to 4. Please see Appendixes B and D for results obtained by different values of  $w_g$  and  $\nabla_{thres}$ , respectively.

#### IV. EXPERIMENTAL RESULTS

We aim to evaluate our decoder from two perspectives: The first is the evaluation as a decoder, specifically whether our decoder can successfully generate images whose features closely match a user-specified feature  $\mathbf{f}_s$ . The second perspective is the evaluation as a feature space analyser, namely whether generated images provide meaningful visual cues about the feature space of the target feature extractor  $f$ . One key issue in designing experiments is determining how to define  $\mathbf{f}_s$  that serves as the goal—that is, the feature of a generated image should be as similar to  $\mathbf{f}_s$  as possible. We define  $\mathbf{f}_s$  as the feature that is extracted from an actual image via  $f$ . This also facilitates the evaluation of the second perspective because we can interpret the adequacy of visual contents in a generated image by referring to the actual image.

The experiments below target three feature extractors to evaluate the generality of our decoder. CLIP's image encoder

with ResNet-50 backbone [6] is selected as the first feature extractor because of its popularity and stability. Then, ResNet-50 is used as the second feature extractor to perform a comparative study against an existing decoder based on a conditional diffusion model [15]. Last, Vision Transformer (ViT) [4] is used as the third feature extractor to compare its feature space with that of less accurate ResNet-50.

By setting  $f$  to each of the three feature extractors described above,  $\mathbf{f}_s$  is extracted from every one of the 15 actual images shown in the leftmost column in Figs. 3 and 4. These images are selected from the dataset used in [26], [27] (the upper three images in Fig. 3), MSCOCO dataset [35] (the five images from the bottom of Fig. 3 and the uppermost image in Fig. 4), and ImageNet dataset [36] (the six images except the uppermost one in Fig. 4). The reason for the small number of image generation attempts is our decoder's computation time as discussed in Section IV-D. Another reason is the limitation of computational resources, as all the experiments were conducted using only one NVIDIA GeForce RTX 3090 with 24GB VRAM and one NVIDIA RTX 4000 Ada with 20GB VRAM. However, as seen from the leftmost column in Figs. 3 and 4, the 15 images encompass a variety of objects (e.g., person, animal, vehicle and food) presented with different backgrounds, so we believe that they are enough for evaluating the overall performance of our decoder.

The hyper-parameters specific to our decoder ( $K$ ,  $T'$  and  $w_g$ ) remain fixed across all the experiments, except for  $\nabla_{thres}$  that is set differently when  $f$  is ViT or the others. Of course, better results might be obtained if finer hyper-parameter tuning were conducted for each experiment. Please see Section III-B for the exact hyper-parameter values. The configuration of the stable diffusion in our decoder is the same as the one in [26], [27].

##### A. Results Targeting CLIP's Image Encoder

Figs. 3 and 4 show images generated by our decoder when using CLIP's image encoder with ResNet-50 backbone as the target feature extractor. For each row,  $\mathbf{f}_s$  is extracted as the

feature of the leftmost actual image and our decoder’s task is to generate an image whose feature is as similar to  $\mathbf{f}_s$  as possible in terms of their squared Euclidean distance. Considering the randomness in generated images, our decoder is run three times. For each run, the following two images are presented: The first is the “finally generated image” that is obtained at the end of the image generation process, and the second is the “best image” whose feature yields the shortest squared Euclidean distance to  $\mathbf{f}_s$  during the image generation process. The number under each generated image shows the squared Euclidean distance between its feature and  $\mathbf{f}_s$ .

First of all, the comparison between the finally generated image and the best one in each run indicates that both of them are visually very similar. However, enriching the best image with detailed contents to produce the finally generated one degrades its squared Euclidean distance and visual similarity to the actual image. Thus, the following discussion focuses only on the best image of each run.

As seen from Figs. 3 and 4, our decoder successfully generates images that have not only very similar features to  $\mathbf{f}_s$  but also similar visual appearances to the actual image from which  $\mathbf{f}_s$  is extracted. Quantitatively, the average pairwise squared Euclidean distance among the 15 actual images in Figs. 3 and 4 is 6.76881 and the one among 10 images that are carefully chosen from the tusker category of ImageNet dataset and confirmed to have similar visual perception by human is 1.40302 (Please see Appendix A for these 10 images). In comparison, the squared Euclidean distance between a best image and its corresponding actual image ranges from 0.02269 (run 2 in the bottom row of Fig. 3) to 0.14704 (run 1 in the second row from the bottom of Fig. 4). This validates our decoder’s ability to generate images each of which has an exceptionally similar feature to  $\mathbf{f}_s$ .

Note that our objective is not to generate realistic images, but rather images whose features closely match  $\mathbf{f}_s$ . This enables us to analyse the feature space of the target feature extractor, more specifically, to investigate what images are located in proximity to the actual image from which  $\mathbf{f}_s$  is extracted. Taking the first row in Fig 3 as an example, each of the generated images—like the actual image—appears to show the same type of dog with a green object around its neck, sitting outdoors with trees in the background (please enlarge the image to see details). But, the dog’s legs and tail are very unnatural, suggesting that CLIP’s image encoder pays little attention to their anatomical topology. Also, the second row in Fig. 3 implies that the feature extracted from the actual image by CLIP’s image encoder only captures a woman with red hair in a visually complex background. Please check the other rows in the same logic. This way, our decoder can offer insights in how image features are extracted by a target feature extractor (CLIP’s image encoder in this experiment) and we believe that these insights are valuable for improving it.

Also, Figs. 3 and 4 demonstrate that the variance among the best images is relatively low. This means that most of the best images closely match the corresponding actual images in terms of their squared Euclidean distances as well as their visual similarities. Although squared Euclidean distances are occasionally unstable as shown in the second row from the

bottom of Fig. 3 and the third row from the top of Fig. 4, all the best images successfully capture the main contents in the corresponding actual images.

### B. Comparative Results Targeting ResNet-50

The main purpose of this experiment is to compare our decoder to Representation Conditional Diffusion Model (RCDM) [15]. RCDM is trained by conditioning its image generation on  $\mathbf{f}_s$  so that a generated image is similar to the actual image from which  $\mathbf{f}_s$  is extracted. In contrast, our decoder requires no training, instead guides the image generation of a pre-trained diffusion model (stable diffusion in this paper). Thus, our aim is to examine which of RCDM or our decoder can generate an image whose feature matches  $\mathbf{f}_s$  more closely.

Figs. 5 and 6 present images generated by our decoder and RCDM. To be precise, ResNet-50 configured with ResNet50\_Weights.IMAGENET1K\_V1<sup>6</sup> is used as the target feature extractor. For each row,  $\mathbf{f}_s$  is defined as the output of the penultimate layer of this ResNet-50 for the leftmost actual image. RCDM used here is actually trained using a large number of images in ImageNet dataset and their features defined in this manner. As in the previous section, our decoder is run three times and the best image for each run is shown. For RCDM, three images through the conditional generation by  $\mathbf{f}_s$  are displayed. The number under each generated image indicates the squared Euclidean distance between its feature and  $\mathbf{f}_s$ .

Figs. 5 and 6 demonstrate that our decoder generates images whose features are much closer to  $\mathbf{f}_s$  than RCDM. Specifically, most of squared Euclidean distances for images generated by our decoder are single-digit while those for RCDM are three-digit. Furthermore, with respect to ResNet-50 features, the average pairwise squared Euclidean distance among the 15 actual images in Figs. 5 and 6 is 715.830 and the one among the 10 tusker images carefully chosen from ImageNet dataset is 171.156 (Please see Appendix A for these images). Based on this, when we make a rough criterion that two images whose squared Euclidean distance is less than 200 are perceptually similar, 22 of the 45 images generated by RCDM in Figs. 5 and 6 are regarded as perceptually similar to their corresponding actual images. On the other hand, all the 45 images generated by our decoder significantly surpass this criterion. Actually, although RCDM can generate images characterised by similar object layouts to the corresponding actual images, the objects in these images are not the same type. This is illustrated by, for instance, dogs in first row of Fig. 5, birds in the second row of Fig. 6 and foods in the third row from the bottom of Fig. 6.

Compared to RCDM, our decoder performs more precise generation of images that capture main contents in the corresponding actual images like object type and background, despite the lack of realness. Again it should be noted that our purpose is not to generate realistic images, but images whose features are close to  $\mathbf{f}_s$  in order to analyse the feature space

<sup>6</sup>[https://docs.pytorch.org/vision/main/models/generated/torchvision.models.resnet50.html#torchvision.models.ResNet50\\_Weights](https://docs.pytorch.org/vision/main/models/generated/torchvision.models.resnet50.html#torchvision.models.ResNet50_Weights)



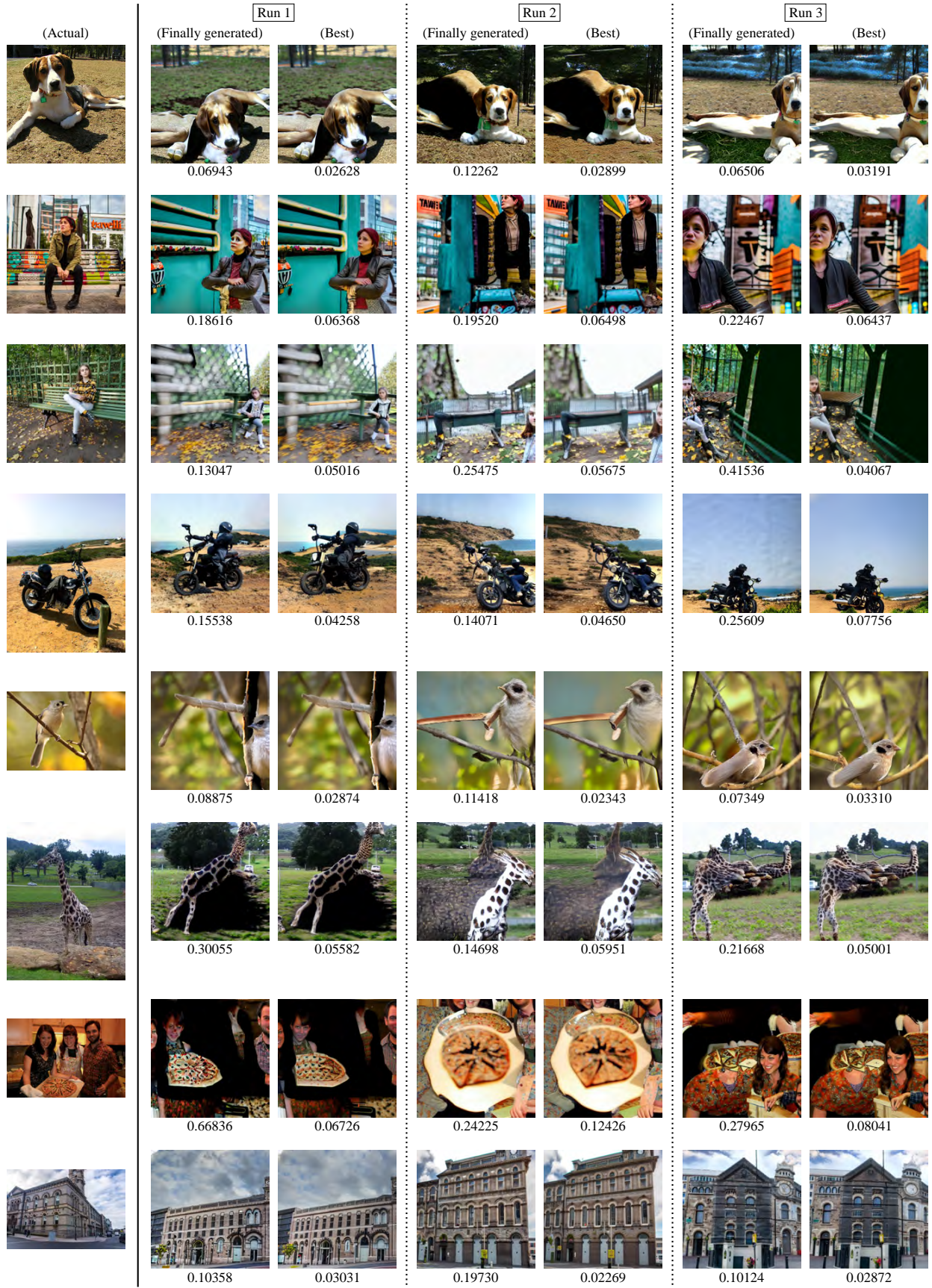


Fig. 3. Images generated by our decoder when using CLIP’s image encoder with ResNet-50 backbone as the target feature extractor. Each row presents three runs of our decoder’s image generation to generate an image whose feature is similar to the one extracted from the leftmost image. For each run, the finally generated image and the best image are shown together with the squared Euclidean distances between their features and the one of the leftmost image.



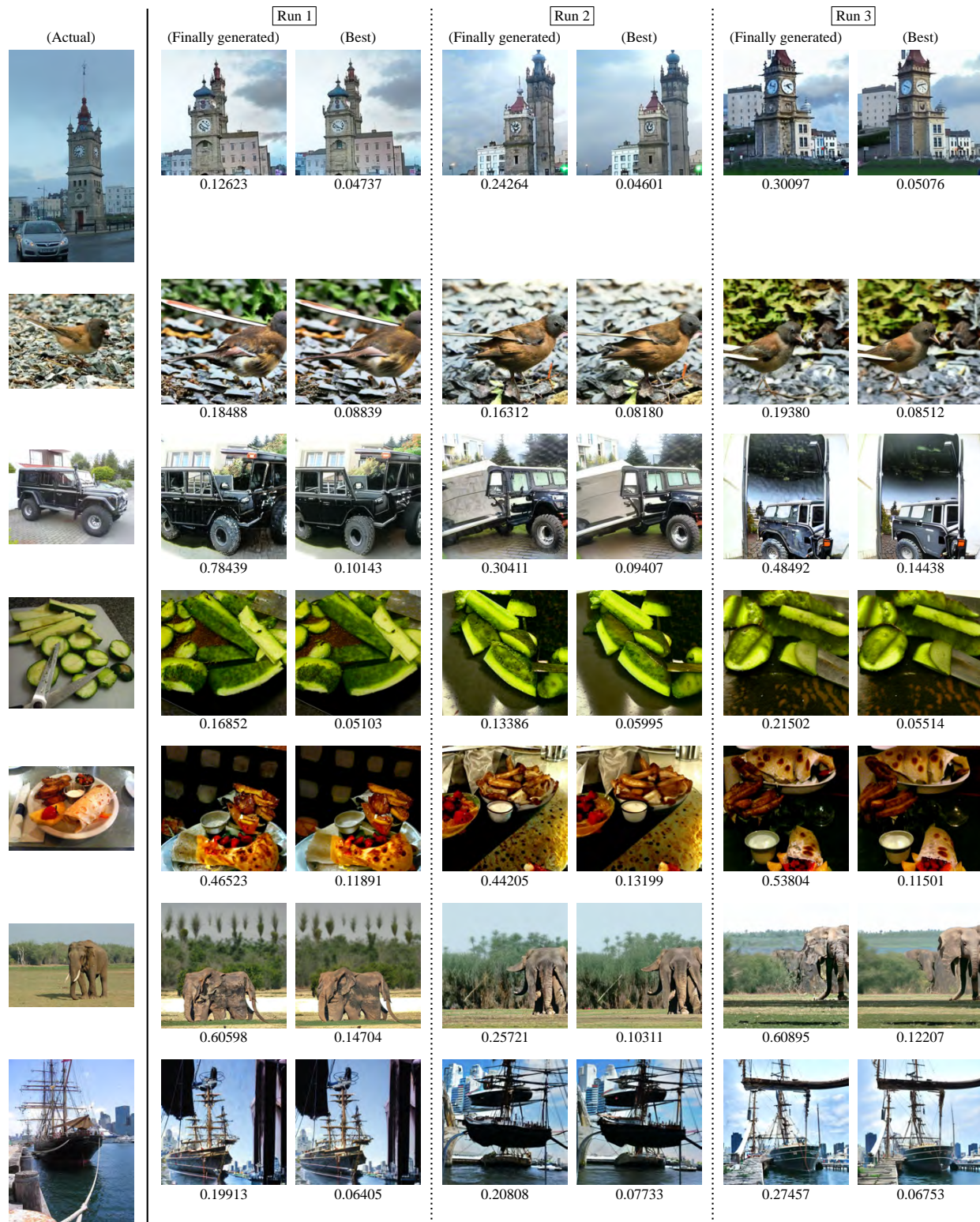


Fig. 4. (Continued from Fig. 3) Images generated by our decoder when using CLIP's image encoder with ResNet-50 backbone as the target feature extractor.



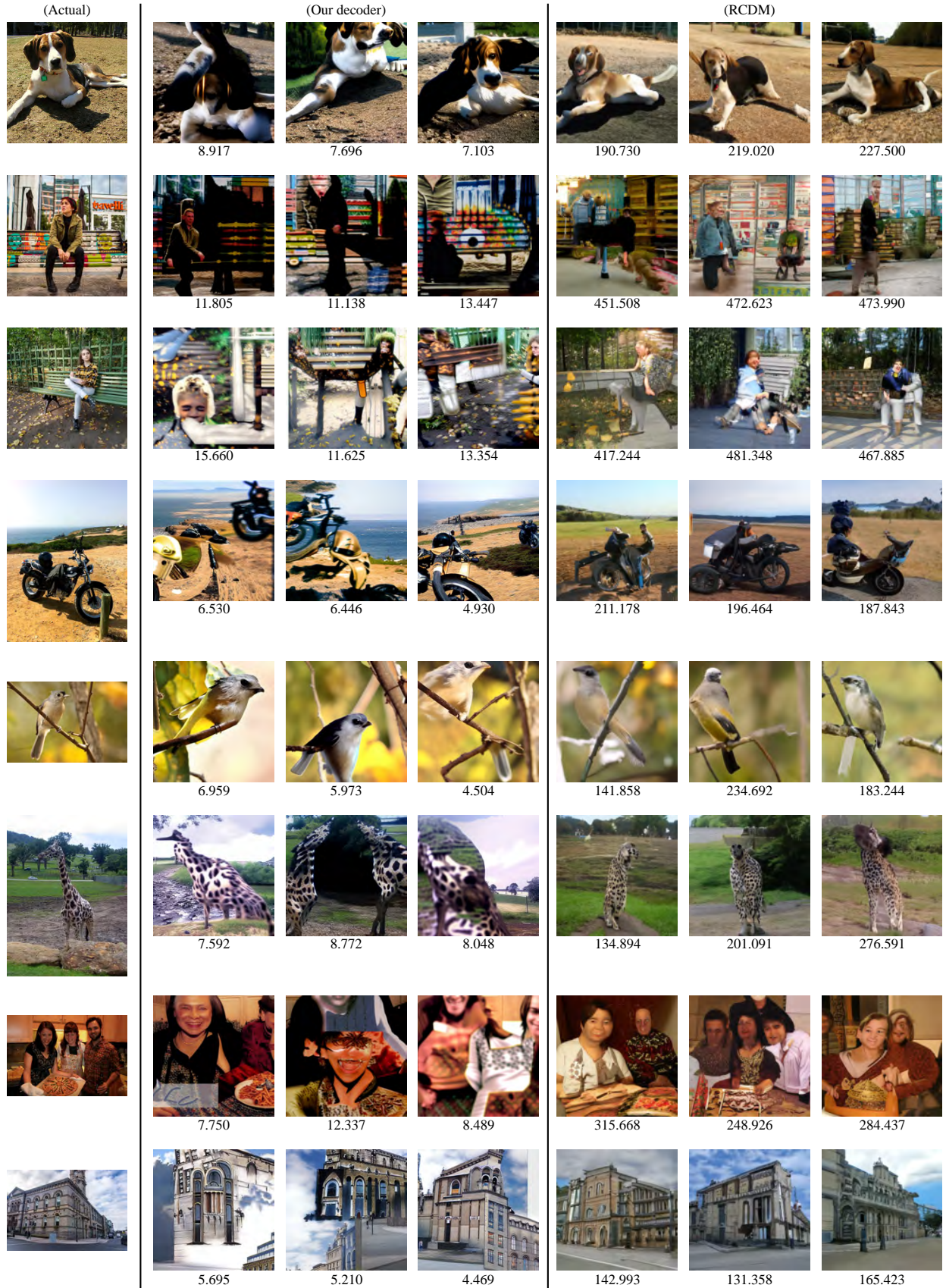


Fig. 5. A comparison between images generated by our decoder and the ones by RCDM when using ResNet-50 as the target feature extractor. For each row, the image generation of our decoder and the one of RCDM are respectively guided and conditioned through the feature extracted from the leftmost actual image. The best images from three respective runs are shown for our decoder while three images generated via the conditional generation are displayed for RCDM. The number under each generated image indicates the squared Euclidean distance between its feature and the one of the corresponding actual image.



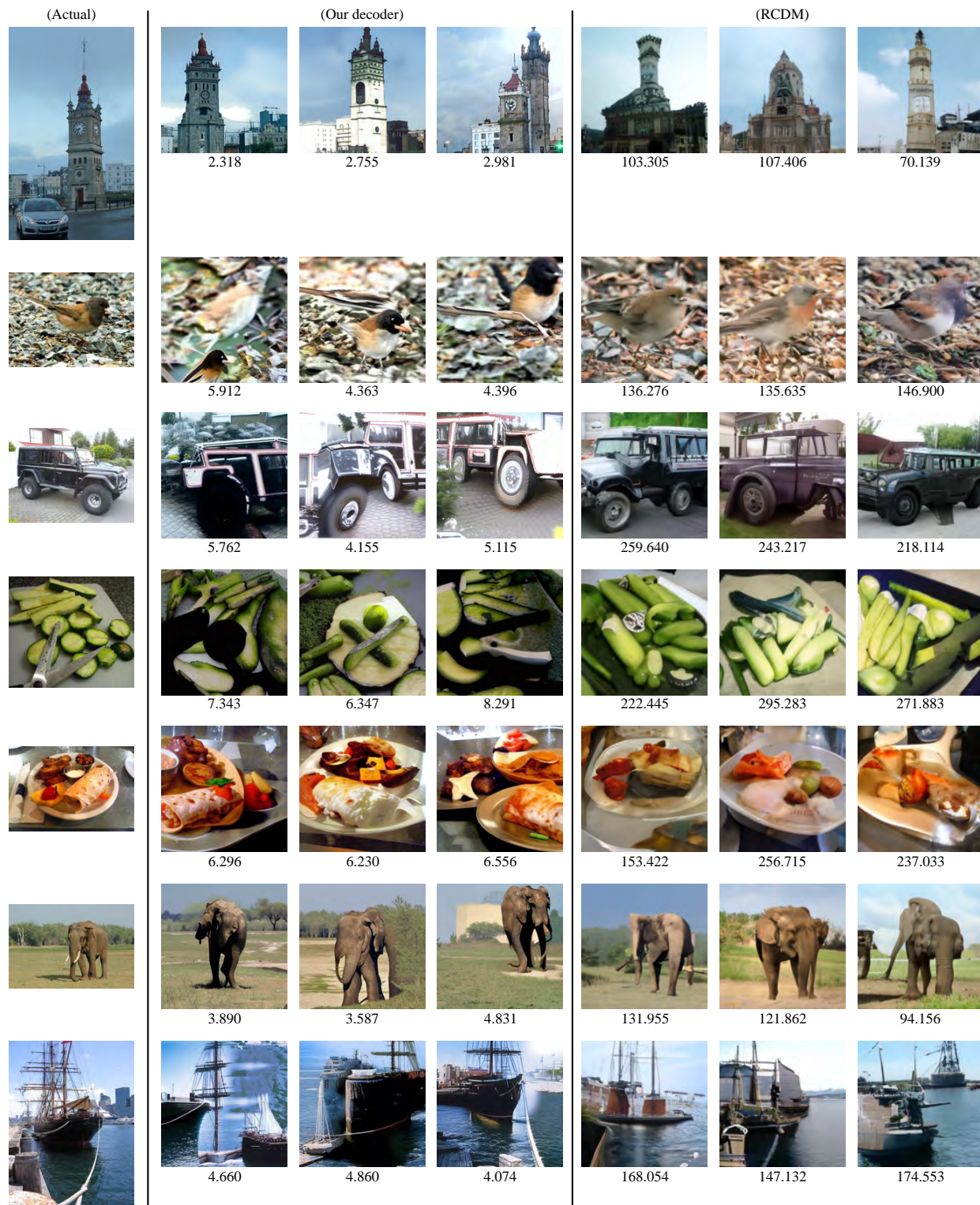


Fig. 6. (Continued from Fig. 5) A comparison between images generated by our decoder and the ones by RCDM when using ResNet-50 as the target feature extractor.

of the target feature extractor (ResNet-50 in this experiment). Conversely, the unrealness of generated images rather implies the imperfectness of the feature space. In addition, the comparison of Figs. 3–6 suggests that the quality of images generated by targeting CLIP’s image encoder seems higher than the one of images generated by targeting ResNet-50. For example, the dogs in the generated images in the top row of Fig. 5 lack green objects around their necks, the cars in the generated images in the third row of Fig. 6 incorrectly include red that is indeed the color of the roof in the background of the actual image, and generated images tend to be poorly formed when the object layout or background is complex, as depicted by the second, third and seventh rows of Fig. 5. We hypothesize that the quality of generated images may be linked to the performance of the target feature extractor and examine this point in the next experiment using ViT that is more accurate than ResNet-50.

### C. Results Targeting ViT-H/14/L

Fig. 7 shows images generated by our decoder when using ViT as the target feature extractor. In particular, ViT-H/14 configured with ViT\_H\_14\_Weights.IMAGENET1K\_SWAG\_E2E\_V1<sup>7</sup> is used because it is ranked at the top in the ranking of the pre-trained models in Pytorch<sup>8</sup>. In this ranking, ResNet-50 used in the previous section achieves a top-1 accuracy of 77.374% on ImageNet-1K classification whereas ViT-H/14 reaches 88.552%. The experiment below aims to examine whether this performance gap is related to images that our decoder generates by targeting ResNet-50 and ViT-H/14. Similar to the experiments before, in Fig. 7,  $f_s$  is extracted by ViT-H/14 from each actual image and the best images obtained by running our decoder three times are displayed next to it. In terms of ViT-H/14 features, the average pairwise squared Euclidean distance among the 15 actual images and the one among the 10 carefully-selected tusker images from ImageNet dataset (please see Appendix A for these images) are 2914.379 and 715.504, respectively. By taking these values as a reference, it can be said that our decoder successfully generates images whose features are remarkably similar to  $f_s$ .

By comparing images generated by targeting ResNet-50 in Figs. 5 and 6 to the ones generated by targeting ViT-H/14 in Figs. 7, the latter clearly preserve more detailed contents in the corresponding actual images than the former. For example, the top row on the left side of Fig. 7 demonstrates that the dogs in the generated images have objects around their necks (although one of them is red), whereas such objects are absent in the generated images in the top row of Fig. 5. In addition, the second row from the bottom on the left side of Fig. 7 shows that the pizzas in the generated images and the actual one look the same. Moreover, as seen from the bottom row on the right side of Fig. 7, both of the generated images and the actual one contain tall buildings in the background (although they appear

to be drawn in the sky in the left generated image). Thus, the preservation of detailed contents in images generated by our decoder can be thought to indicate the usefulness of features extracted by the target feature extractor. This corresponds to [13]’s conclusion that features (logit vectors) extracted by a better image classification model retains richer information.

Regarding the comparison between CLIP’s image encoder with ResNet-50 backbone in Section IV-A and ViT-H/14 in this section, the latter is expected to outperform the former on ImageNet-1K classification. The reason is that even if a more advanced CLIP’s image encoder with ViT-Large/14 backbone is carefully finetuned on ImageNet-1K dataset, its top-1 accuracy is 88.0% [37], which is lower than the one (88.552%) of ViT-H/14 in this section. Correspondingly, the generated images in Fig. 7 seem better than the ones in Figs. 3 and 4 in terms of the preservation of detailed contents, as seen by comparing birds and foods in these images. However, the main advantage of CLIP’s image encoder is its zero-shot performance, that is, the generality of features extracted by it. As represented by the six actual images from the bottom on the right side of Fig. 7, most of images in ImageNet-1K dataset prominently display the main object near the centre. Thus, when targeting ViT-H/14 trained on such images, generated images tend to spend a large region for the main object and lose its surrounding context. In contrast, as can be seen from Figs. 3 and 4, such a surrounding context is better preserved in the images generated by targeting CLIP’s image encoder. This context preservation could be one indicator of the generality of features extracted by the target feature extractor.

### D. Discussions

This section presents four issues observed from the experiments before and discuss research topics that warrant further investigation. In particular, the first two issues are for the improvement of our decoder and the remaining two are for the construction of a better feature space.

1) *Enhancing the loss function of our decoder*: It can be hypothesised that if we could improve our decoder to generate more realistic and natural images, those images would be located in closer proximity to the corresponding actual image in the feature space, compared images generated in this paper. As observed in images generated by targeting ViT-H/14 in Fig. 7, one typical artifact making generated images unrealistic and unnatural is large black regions, resulting from excessive modification of the predicted source noise  $\epsilon_\theta(z_t, t)$  in Eq. (3) (Appendix D presents how gradient clipping mitigates this artifact). When a large region in an image is spent for such artifacts, only the remaining region can be used to make its feature match a user-specified one, which significantly limits the possibility of images that can be generated. One promising solution is to enhance the loss function by adopting a perceptual quality assessment of a generated image [38], [39] in addition to the squared Euclidean distance between its feature and the user-specified one. This reduces artifact creation and enables our decoder to use the entire image region, increasing the possibility of a close feature match.

<sup>7</sup>[https://docs.pytorch.org/vision/main/models/generated/torchvision.models.vit\\_h\\_14.html#torchvision.models.ViT\\_H\\_14\\_Weights](https://docs.pytorch.org/vision/main/models/generated/torchvision.models.vit_h_14.html#torchvision.models.ViT_H_14_Weights)

<sup>8</sup><https://docs.pytorch.org/vision/main/models.html#table-of-all-available-classification-weights> (accessed on July 30, 2025)



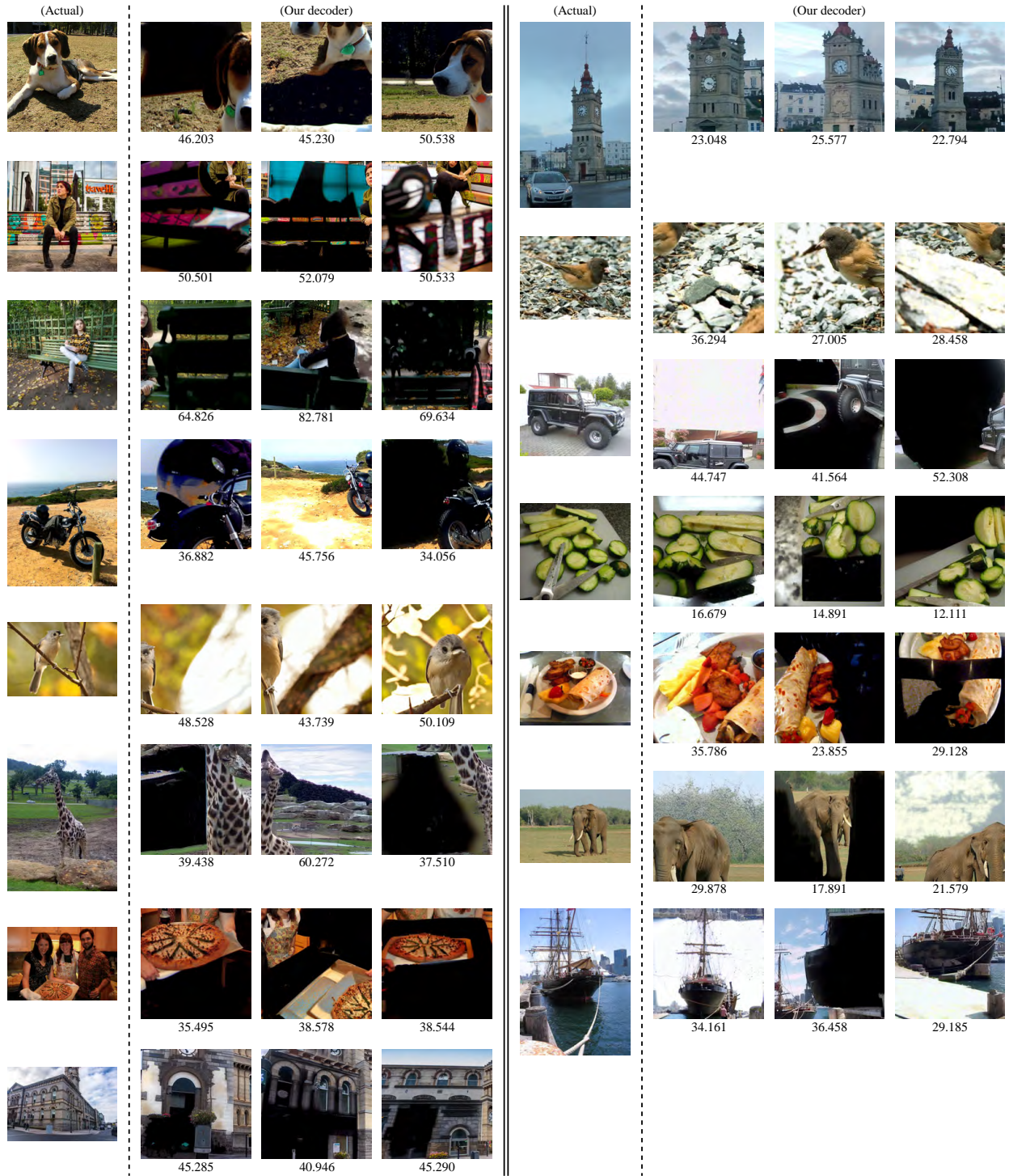


Fig. 7. Images generated by our decoder when using ViT-H/14 as the target feature extractor. For each actual image, our decoder is run three times and the best image in each run is shown with the squared Euclidean distance between its feature and the one of the actual image.

2) *Reducing the computation time of our decoder*: One drawback of our decoder is its computation time. Specifically, NVIDIA GeForce RTX 3090 was used to generate the images in Figs. 3 and 4 by targeting CLIP’s image encoder with ResNet-50 backbone and the average computation time per image generation run is 8830 seconds. Using the same GPU, the images in Figs. 5 and 6 were generated by targeting ResNet-50 with an average computation time of 8951 seconds per run. The images generated by targeting ViT-H/14 in Fig. 7 were generated using NVIDIA GeForce RTX 3090 and NVIDIA RTX 4000 Ada, which required on average 16897 and 22694 seconds per run, respectively. One solution for reducing these computation times<sup>9</sup> is to implement our decoder on a fast sampler that can be incorporated into a pre-trained diffusion model to generate images with a small number of steps [40], [41].

3) *Smooth alignment between features and visual appearances*: One main finding from the experiments before is that unrealistic and unnatural images (generated by our decoder) are located in close proximity to an actual image in the feature space. Although these generated images capture the main characteristics of the actual image, they exhibit limited visual similarity. This suggests a potential direction for improving current feature extractors, that is, it may be possible to design a training objective that enforces a smooth transition in visual appearances of images according to their Euclidean distances in the feature space.

4) *Suitability of CLIP’s multimodal feature space*: Since CLIP is a visual-semantic embedding model that can directly measure similarities between images and textual captions by projecting them into a common feature (embedding) space, one interesting question is what kind of image has the same feature to the one of a caption. To check this, our decoder is run to generate an image whose feature closely matches the one of a caption. As shown in the columns named “Caption” and “Actual” in Fig. 8, we use captions that are assigned to the actual images in MSCOCO dataset. In other words, we aim to examine whether an image generated by defining  $f_s$  as the feature of a caption is similar to the corresponding actual image. As seen from the column named “Original”, generated images are completely different from their corresponding actual images, and their features exhibit huge squared Euclidean distances to those of the corresponding captions.

Let us investigate the reason for the aforementioned result. First, CLIP is trained so that an image and the caption assigned to it are close in the feature space with respect to their (normalised) cosine similarity, not their squared Euclidean distance [6]. Thus, despite their directional similarity, they are located in completely different regions in the feature space, as verified by the fact that the average norm of the features of the six actual images in Fig. 8 and the one of the corresponding six captions are 2.177 and 9.795, respectively. This motivates us to run our decoder to generate an image by defining  $f_s$  as the caption’s normalised feature whose norm is equal to the average feature norm of the six actual images. Nonetheless,

the column named “Normalised” in Fig. 8 shows that the generated images significantly differ from the corresponding actual images, although they slightly align with the captions as typically observed in the second image from the bottom.

The above failure of generating reasonable images is not due to our decoder. The columns named “ $\times 1.2$ ” and “ $\times 0.8$ ” present images generated by setting  $f_s$  to 1.2 and 0.8 times the feature of the corresponding actual image, respectively. The hypothesis for this is that the generated images and the actual one have the same normalised cosine similarity to the caption in terms of their features and should be semantically relevant to the caption. The images generated by our decoder appear to support this hypothesis. Thus, as long as there exist real images in proximity to a user-specified feature, our decoder can generate reasonable images capturing the main contents in those images. Therefore, we conclude that the huge Euclidean distance between the feature of each caption and that of the generated image suggests no existence of real images having this caption’s feature. Although the Euclidean distance could be reduced to some extent by changing the backbone diffusion model of our decoder from stable diffusion to a more advanced one, our conclusion is likely to remain valid. Like this, images and captions are located in completely different regions of CLIP’s feature space<sup>10</sup> although relevant image-caption pairs have relatively high angular similarities. It would be an important research topic to examine the suitability of such a multimodal feature space where images are only weakly associated with relevant captions.

## V. CONCLUSION AND FUTURE WORK

This paper introduced a decoder that generates images whose features are ensured to closely match user-specified ones. Owing to the short Euclidean distances between these features, we can perform rigorous analysis of the feature space of a target feature extractor. Our decoder is implemented as a guided diffusion model that needs no training, instead guides a pre-trained diffusion model (stable diffusion in this paper) to minimise the squared Euclidean distance between the feature of a generated image and the user-specified one. Furthermore, the early step emphasis strategy and gradient normalisation and clipping are devised to improve our decoder’s image generation. The experiments using each of CLIP’s image encoder with ResNet-50 backbone, ResNet-50 and ViT-H/14 as the target feature extractor demonstrate that images generated by our decoder have features remarkably similar to the specified ones and offer valuable insights into the feature space of the extractor.

In addition to the four issues discussed in Section IV-D, we plan to implement our decoder on pre-trained diffusion models other than stable diffusion and to analyse feature spaces of more recent feature extractors than the ones employed in this paper (e.g., image encoders implemented in OpenCLIP project [42]). Also, we aim to improve our decoder’s image generation by formulating the guidance-based reverse process

<sup>9</sup>Our decoder consumes about 15.1, 14.9 and 19.6GB of VRAM for image generation runs targeting CLIP’s image encoder with ResNet-50 backbone, ResNet-50 and ViT-H/14, respectively.

<sup>10</sup>This can be thought as the reason why the CLIP-based text-to-image in [14] first converts the feature of a text prompt into the corresponding image feature.





Fig. 8. Images generated by our decoder when using CLIP’s image encoder with ResNet-50 backbone as the target feature extractor. For the second and third columns,  $\mathbf{f}_s$  is defined as the feature of each caption and its normalised one, respectively. On the other hand,  $\mathbf{f}_s$  is set to 1.2 and 0.8 times the feature of each actual image. The number under each generated image indicates the squared Euclidean distance between its feature and  $\mathbf{f}_s$  used to generated it.



as a search problem to find the optimal sequence of denoising operations [43], [44]. Finally, our encoder can be readily extended to other modalities like text, audio and time-series to analyse their respective feature spaces.

## APPENDIX A

### 10 CAREFULLY-CHOSEN TUSKER IMAGES

Fig. 9 shows the 10 images used to compute the average squared Euclidean distance, which can be a reference to interpret how close the feature of an image generated by our decoder is to a user-specified feature.



Fig. 9. 10 images that are carefully chosen from the tusker category of ImageNet dataset and validated by human to exhibit similar visual perception.

## APPENDIX B

### EFFECT OF $w_g$

To check the effect of  $w_g$  in Eq. (3), this experiment aims to investigate a transition of squared Euclidean distances between features of generated images and the ones of their corresponding actual images on  $w_g$  values of 0.5, 1, 2, 4 and 8. Specifically, using CLIP's image encoder with ResNet-50 backbone as the target feature extractor,  $\mathbf{f}_s$  is defined as the feature of each of the 15 actual images in Figs. 3 and 4. Except  $w_g$ , all the other hyper-parameters are fixed as configured in Section III-B. Similar to the experiments before, this experiment targets the best image whose feature yields the shortest squared Euclidean distance to  $\mathbf{f}_s$  in the image generation process.

Fig. 10 depicts a box plot that summarises the median, 25 and 75 percentiles, and the maximum and minimum of squared Euclidean distances between the features of the 15 best images generated by each  $w_g$  value and the ones of the corresponding actual images. As seen from Fig. 10,  $w_g = 8$  leads to images whose features exhibit shorter squared Euclidean distances than  $w_g = 4$  used in Section IV. Regarding this, Figs. 11 and 12 presents the images generated by each  $w_g$  value. As can be seen from the top row and the second row from the bottom of Fig. 11 and the second row from the bottom of Fig. 12,  $w_g = 8$  sometimes results in too unrealistic images despite the short squared Euclidean distances. This can hinder the feature space analysis by visually checking generated images. Thus,  $w_g = 4$  is adopted to balance between minimising squared Euclidean distances and maintaining the realness of generated images.

## APPENDIX C

### EFFECT OF THE EARLY STEP EMPHASIS STRATEGY

Using  $w_g = 4$  in Appendix B, an ablation study is conducted to compare image generation approaches with and

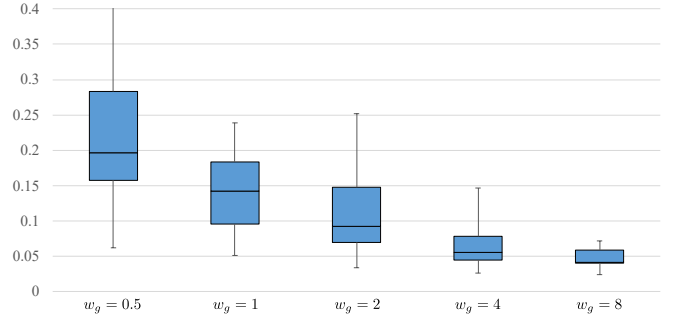


Fig. 10. A box-plot of squared Euclidean distances between features of generated images and the ones of their corresponding actual images on different  $w_g$  values when using CLIP's image encoder with ResNet-50 backbone as the target feature extractor.

without the early step emphasis strategy. That is, the former uses  $K = 1000$  and  $K = 8$  self-recurrence iterations at the first  $T' = 5$  reverse steps and the others, respectively, whereas the latter uses  $K = 8$  at all steps. When using the early step emphasis strategy, the average squared Euclidean distance between the features of the 15 generated images in Figs. 11 and 12 and the ones of the corresponding actual images is  $0.06554 \pm 0.03468$ . In contrast, without this strategy, the average is  $0.06906 \pm 0.03185$ . This verifies the effectiveness of the early step emphasis strategy for generating images whose features match user-specified ones more closely.

## APPENDIX D

### EFFECT OF $\nabla_{thres}$

To demonstrate  $\nabla_{thres}$ 's effect on our decoder's image generation, Fig. 13 shows images generated by setting  $\nabla_{thres}$  to three times the standard deviation of values in  $\nabla_{z_t} l(f(\hat{\mathbf{x}}_t), \mathbf{f}_s)$  when using ViT-H/14 as the target feature extractor. As seen from Fig. 13, a generated image often contains an artifactual (unintended) large black region that is caused by Eq. (3) where the predicted source noise  $\epsilon_\theta(z_t, t)$  is excessively modified with large gradient values in  $\nabla_{z_t} l(f(\hat{\mathbf{x}}_t), \mathbf{f}_s)$ . The maximum gradient value used in this modification is reduced using a smaller  $\nabla_{thres}$  like twice the standard deviation of values in  $\nabla_{z_t} l(f(\hat{\mathbf{x}}_t), \mathbf{f}_s)$ , as is the case for Fig. 7. As a result, a generated image becomes less likely to contain an artifactual large black region, although several images in Fig. 7 still have such regions. In addition, setting  $\nabla_{thres}$  to a further lower value prevents our decoder from generating images whose features are sufficiently close to a user-specified feature. One possible solution for artifactual large black regions is discussed in Section IV-D.

## REFERENCES

- [1] Y. Bengio, A. Courville, and P. Vincent, "Representation learning: A review and new perspectives," *IEEE Trans. Pattern Anal. Mach. Intell.*, vol. 35, no. 8, p. 1798–1828, 2013.
- [2] F. Li, K. Shirahama, M. A. Nisar, L. Köping, and M. Grzegorzec, "Comparison of feature learning methods for human activity recognition using wearable sensors," *Sensors*, vol. 18, no. 2, 2018.
- [3] K. He, X. Zhang, S. Ren, and J. Sun, "Deep residual learning for image recognition," in *Proc. of the 2016 IEEE Conference on Computer Vision and Pattern Recognition (CVPR 2016)*, 2016, pp. 770–778.

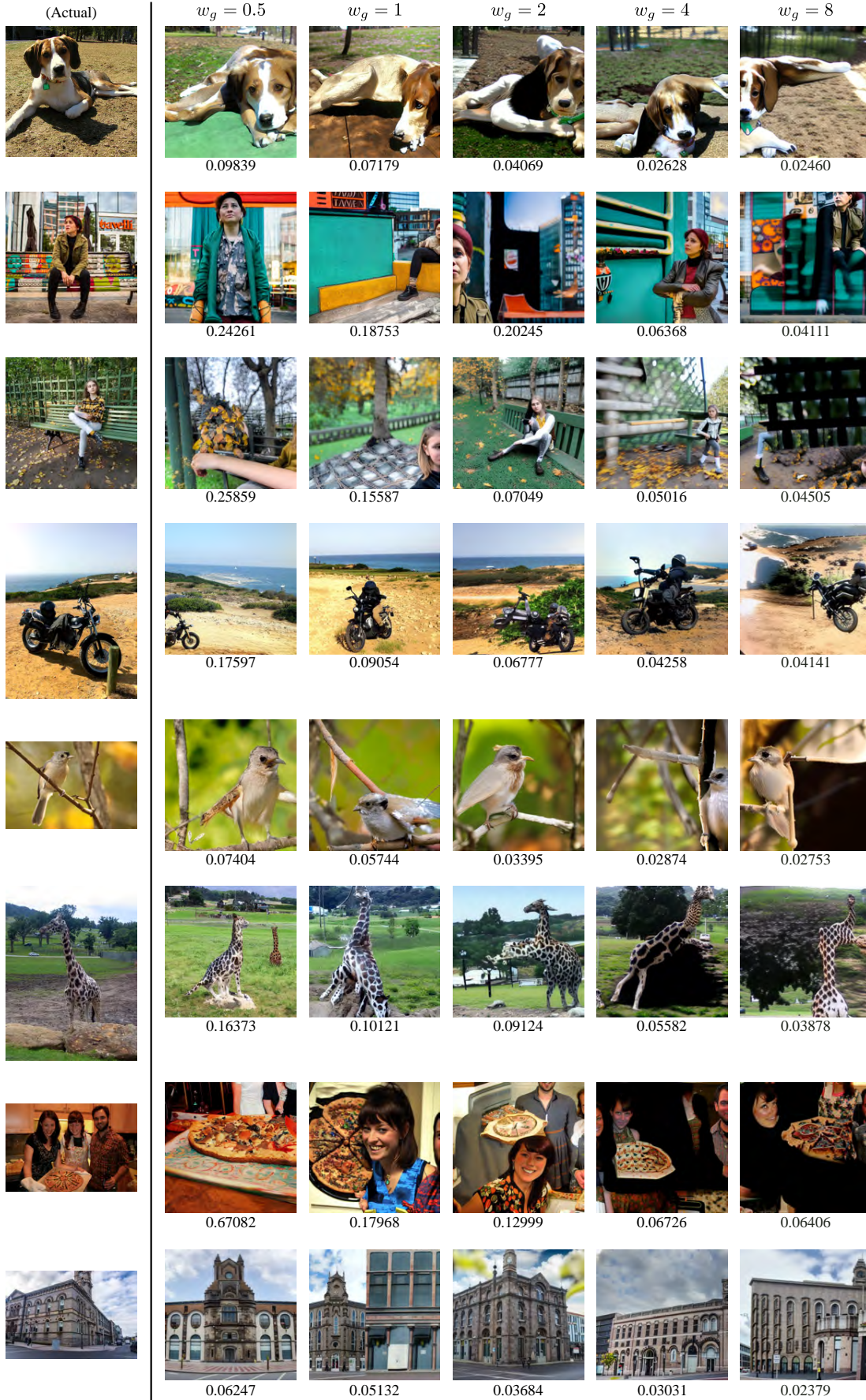


Fig. 11. Images generated by our decoder with  $w_g$  values of 0.5, 1, 2, 4 and 8 when using CLIP's image encoder with ResNet-50 backbone as the target feature extractor. The best image in each image generation run is shown with the squared Euclidean distance between its feature and the one of the corresponding actual image.



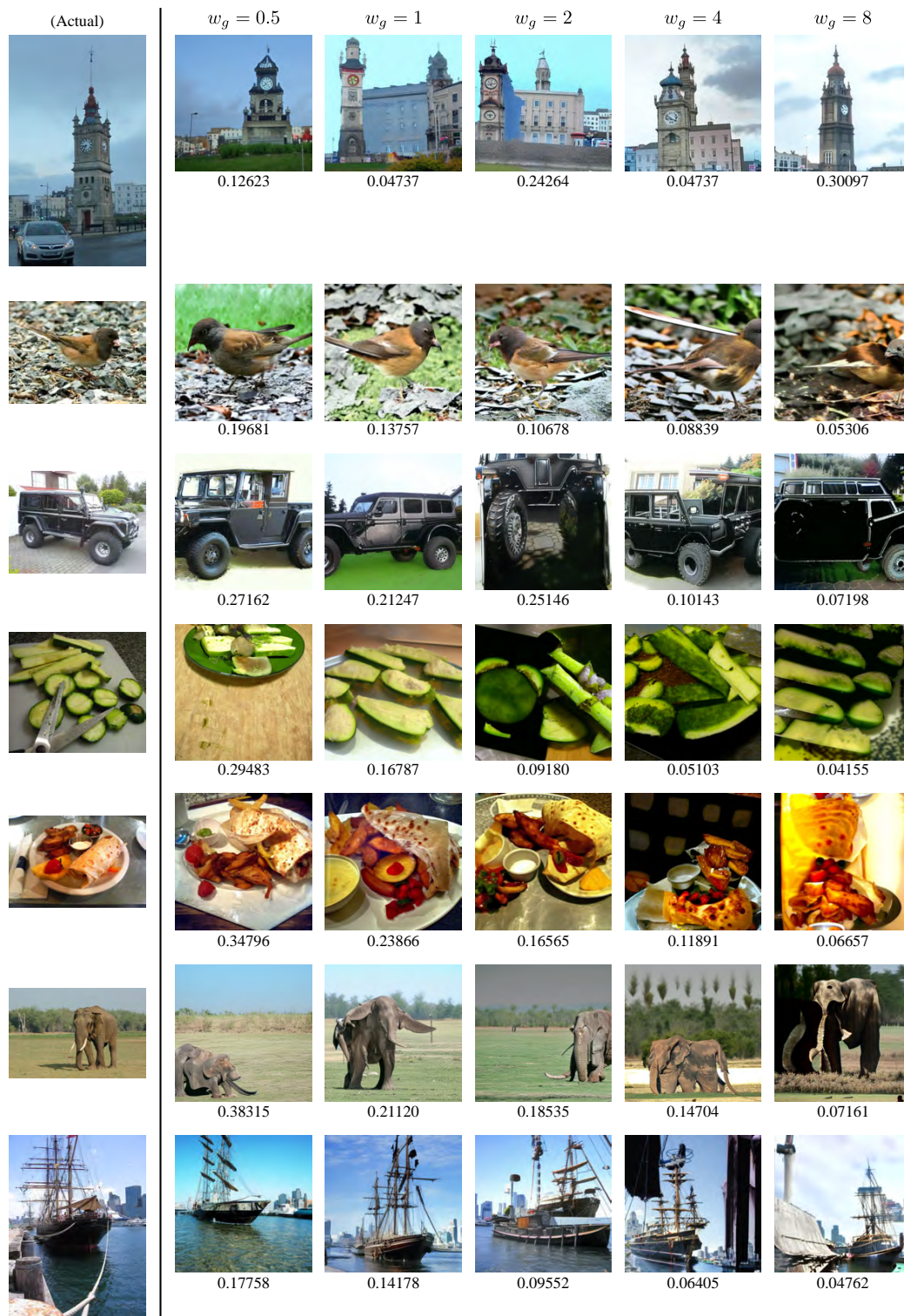


Fig. 12. (Continued from Fig. 12) Images generated by our decoder with  $w_g$  values of 0.5, 1, 2, 4 and 8 when using CLIP's image encoder with ResNet-50 backbone as the target feature extractor..



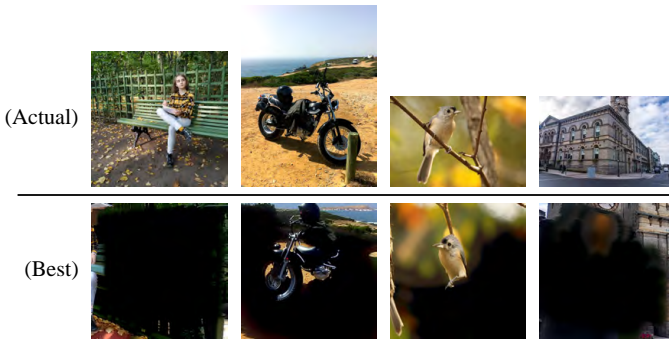


Fig. 13. Example images generated by our decoder when using ViT-H/14 as the target feature extractor and set  $\nabla_{thres}$  to three times the standard deviation of values in  $\nabla_{z_t} l(f(\hat{x}_t), f_s)$ .

- [4] A. Dosovitskiy, L. Beyer, A. Kolesnikov, D. Weissenborn, X. Zhai, T. Unterthiner, M. Dehghani, M. Minderer, G. Heigold, S. Gelly, J. Uszkoreit, and N. Houlsby, “An image is worth 16x16 words: Transformers for image recognition at scale,” in *Proc. of the Ninth International Conference on Learning Representations (ICLR 2021)*, 2021.
- [5] F. Faghri, D. J. Fleet, J. R. Kiros, and S. Fidler, “Vse++: Improving visual-semantic embeddings with hard negatives,” in *Proc. of the 29th British Machine Vision Conference (BMVC 2018)*, 2018.
- [6] A. Radford, J. W. Kim, C. Hallacy, A. Ramesh, G. Goh, S. Agarwal, G. Sastry, A. Askell, P. Mishkin, J. Clark, G. Krueger, and I. Sutskever, “Learning transferable visual models from natural language supervision,” in *Proc. of the 38th International Conference on Machine Learning (ICML 2021)*, 2021, pp. 8748–8763.
- [7] J. Donahue, L. A. Hendricks, M. Rohrbach, S. Venugopalan, S. Guadarrama, K. Saenko, and T. Darrell, “Long-term recurrent convolutional networks for visual recognition and description,” *IEEE Trans. Pattern Anal. Mach. Intell.*, vol. 39, no. 4, p. 677–691, 2017.
- [8] P. Isola, J.-Y. Zhu, T. Zhou, and A. A. Efros, “Image-to-image translation with conditional adversarial networks,” in *Proc. of the 2017 IEEE Conference on Computer Vision and Pattern Recognition (CVPR 2017)*, 2017, pp. 5967–5976.
- [9] A. Hertz, R. Mokady, J. Tenenbaum, K. Aberman, Y. Pritch, and D. Cohen-or, “Language model inversion,” in *Proc. of the 11th International Conference on Learning Representations (ICLR 2023)*, 2023.
- [10] V. Feldman and C. Zhang, “What neural networks memorize and why: discovering the long tail via influence estimation,” in *Proc. of the 34th International Conference on Neural Information Processing Systems (NeurIPS 2020)*, 2020.
- [11] K. Tirumala, A. Markosyan, L. Zettlemoyer, and A. Aghajanyan, “Memorization without overfitting: Analyzing the training dynamics of large language models,” in *Proc. of the 36th International Conference on Neural Information Processing Systems (NeurIPS 2022)*, 2022.
- [12] R. Bansal, D. Pruthi, and Y. Belinkov, “Measures of information reflect memorization patterns,” in *Proceedings of the 36th International Conference on Neural Information Processing Systems (NeurIPS 2022)*, 2022.
- [13] P. Teterwak, C. Zhang, D. Krishnan, and M. C. Mozer, “Understanding invariance via feedforward inversion of discriminatively trained classifiers,” in *Proc. of the 38th International Conference on Machine Learning (ICML 2021)*, 2021, pp. 10225–10235.
- [14] A. Ramesh, P. Dhariwal, A. Nichol, C. Chu, and M. Chen, “Hierarchical Text-Conditional Image Generation with CLIP Latents,” *arXiv e-prints arXiv:2204.06125*, 2022.
- [15] F. Bordes, R. Balestriero, and P. Vincent, “High fidelity visualization of what your self-supervised representation knows about,” *Transactions on Machine Learning Research*, 2022. [Online]. Available: <https://openreview.net/forum?id=urfWb7VjmL>
- [16] J. Ho, A. Jain, and P. Abbeel, “Denoising diffusion probabilistic models,” in *Proc. of the 34th International Conference on Neural Information Processing Systems (NeurIPS 2020)*, 2020.
- [17] R. Rombach, A. Blattmann, D. Lorenz, P. Esser, and B. Ommer, “High-resolution image synthesis with latent diffusion models,” in *Proc. of the 2022 IEEE/CVF Conference on Computer Vision and Pattern Recognition (CVPR 2022)*, 2022, pp. 10674–10685.
- [18] P. Dhariwal and A. Nichol, “Diffusion models beat gans on image synthesis,” in *Proc. of the 35th International Conference on Neural Information Processing Systems (NeurIPS 2021)*, 2021.
- [19] J. Ho and T. Salimans, “Classifier-free diffusion guidance,” in *Proc. of the NeurIPS 2021 Workshop on Deep Generative Models and Downstream Applications (DGMs and Applications @ NeurIPS 2021)*, 2021.
- [20] A. Q. Nichol, P. Dhariwal, A. Ramesh, P. Shyam, P. Mishkin, B. McGrew, I. Sutskever, and M. Chen, “GLIDE: Towards photorealistic image generation and editing with text-guided diffusion models,” in *Proc. of the 39th International Conference on Machine Learning (ICML 2022)*, 2022, pp. 16784–16804.
- [21] A. Graikos, N. Malkin, N. Jojic, and D. Samaras, “Diffusion models as plug-and-play priors,” in *Proc. of the 36th International Conference on Neural Information Processing Systems (NeurIPS 2022)*, 2022.
- [22] H. Chefer, Y. Alaluf, Y. Vinker, L. Wolf, and D. Cohen-Or, “Attend-and-excite: Attention-based semantic guidance for text-to-image diffusion models,” *ACM Trans. Graph.*, vol. 42, no. 4, 2023.
- [23] D. Epstein, A. Jabri, B. Poole, A. A. Efros, and A. Holynski, “Diffusion self-guidance for controllable image generation,” in *Proc. of the 37th International Conference on Neural Information Processing Systems (NeurIPS 2023)*, 2023.
- [24] G. Kim, W. Jang, G. Lee, S. Hong, J. Seo, and S. Kim, “Depth-aware guidance with self-estimated depth representations of diffusion models,” *Pattern Recogn.*, vol. 153, no. C, 2024.
- [25] K. Sueyoshi and T. Matsubara, “Predicated diffusion: Predicate logic-based attention guidance for text-to-image diffusion models,” in *Proc. of the 2024 IEEE/CVF Conference on Computer Vision and Pattern Recognition (CVPR 2024)*, 2024, pp. 8651–8660.
- [26] A. Bansal, H.-M. Chu, A. Schwarzschild, R. Sengupta, M. Goldblum, J. Geiping, and T. Goldstein, “Universal guidance for diffusion models,” in *Proc. of the 12th International Conference on Learning Representations (ICLR 2024)*, 2024.
- [27] A. Bansal, H.-M. Chu, A. Schwarzschild, S. Sengupta, M. Goldblum, J. Geiping, and T. Goldstein, “Universal guidance for diffusion models,” in *Proc. of the 2023 IEEE/CVF Conference on Computer Vision and Pattern Recognition Workshops (CVPRW)*, 2023, pp. 843–852.
- [28] Z. Wang, Y. Jiang, H. Zheng, P. Wang, P. He, Z. Wang, W. Chen, and M. Zhou, “Patch diffusion: faster and more data-efficient training of diffusion models,” in *Proc. of the 37th International Conference on Neural Information Processing Systems (NeurIPS 2023)*, 2023.
- [29] H. Zheng, W. Nie, A. Vahdat, and A. Anandkumar, “Fast training of diffusion models with masked transformers,” *Transactions on Machine Learning Research*, 2024. [Online]. Available: <https://openreview.net/forum?id=vTBjBtGioE>
- [30] J. X. Morris, W. Zhao, J. T. Chiu, V. Shmatikov, and A. M. Rush, “Language model inversion,” in *Proc. of the 12th International Conference on Learning Representations (ICLR 2024)*, 2024.
- [31] J. Morris, V. Kuleshov, V. Shmatikov, and A. Rush, “Text embeddings reveal (almost) as much as text,” in *Proc. of the 2023 Conference on Empirical Methods in Natural Language Processing (ACL 2023)*, 2023, pp. 12448–12460.
- [32] A. Lugmayr, M. Danelljan, A. Romero, F. Yu, R. Timofte, and L. Van Gool, “Repaint: Inpainting using denoising diffusion probabilistic models,” in *Proc. of the 2022 IEEE/CVF Conference on Computer Vision and Pattern Recognition (CVPR 2022)*, 2022, pp. 11451–11461.
- [33] Y. Wang, J. Yu, and J. Zhang, “Zero-shot image restoration using denoising diffusion null-space model,” in *Proc. of the 11th International Conference on Learning Representations (ICLR 2023)*, 2023.
- [34] L. Liu, C. Dong, X. Liu, B. Yu, and J. Gao, “Bridging discrete and backpropagation: straight-through and beyond,” in *Proc. of the 37th International Conference on Neural Information Processing Systems (NeurIPS 2023)*, 2023.
- [35] T.-Y. Lin, M. Maire, S. Belongie, J. Hays, P. Perona, D. Ramanan, P. Dollár, and C. L. Zitnick, “Microsoft coco: Common objects in context,” in *Proc. of the 13th European Conference on Computer Vision (ECCV 2014)*, 2014, pp. 740–755.
- [36] O. Russakovsky, J. Deng, H. Su, J. Krause, S. Satheesh, S. Ma, Z. Huang, A. Karpathy, A. Khosla, M. Bernstein, A. C. Berg, and L. Fei-Fei, “Imagenet large scale visual recognition challenge,” *International Journal of Computer Vision*, vol. 115, no. 3, p. 211–252, 2015.
- [37] X. Dong, J. Bao, T. Zhang, D. Chen, S. Gu, W. Zhang, L. Yuan, D. Chen, F. Wen, and N. Yu, “CLIP itself is a Strong Fine-tuner: Achieving 85.7% and 88.0% Top-1 Accuracy with ViT-B and ViT-L on ImageNet,” *arXiv e-prints arXiv:2212.06138*, 2022.
- [38] R. Zhang, P. Isola, A. A. Efros, E. Shechtman, and O. Wang, “The unreasonable effectiveness of deep features as a perceptual metric,”

- in *Proc. of the 2018 IEEE/CVF Conference on Computer Vision and Pattern Recognition (CVPR 2018)*, 2018, pp. 586–595.
- [39] J. Wang, K. C. Chan, and C. C. Loy, “Exploring clip for assessing the look and feel of images,” in *Proc. of the 37th AAAI Conference on Artificial Intelligence (AAAI 2023)*, 2023, pp. 2555–2563.
- [40] J. Song, C. Meng, and S. Ermon, “Denoising diffusion implicit models,” in *Proc. of the Ninth International Conference on Learning Representations (ICLR 2021)*, 2021.
- [41] W. Zhao, L. Bai, Y. Rao, J. Zhou, and J. Lu, “Unipc: a unified predictor-corrector framework for fast sampling of diffusion models,” in *Proc. of the 37th International Conference on Neural Information Processing Systems*, 2023.
- [42] G. Ilharco, M. Wortsman, R. Wightman, C. Gordon, N. Carlini, R. Taori, A. Dave, V. Shankar, H. Namkoong, J. Miller, H. Hajishirzi, A. Farhadi, and L. Schmidt, “Openclip,” 2021, Zenodo. [Online]. Available: <https://doi.org/10.5281/zenodo.5143773>
- [43] N. Ma, S. Tong, H. Jia, H. Hu, Y.-C. Su, M. Zhang, X. Yang, Y. Li, T. Jaakkola, X. Jia, and S. Xie, “Inference-Time Scaling for Diffusion Models beyond Scaling Denoising Steps,” *arXiv e-prints arXiv:2501.09732*, 2025.
- [44] V. Ramesh and M. Mardani, “Test-Time Scaling of Diffusion Models via Noise Trajectory Search,” *arXiv e-prints arXiv:2506.03164*, 2025.

**Kimiaki Shirahama** Kimiaki Shirahama received the B.E., M.E., and D.E. degrees in engineering from Kobe University, Japan, in 2003, 2005, and 2011, respectively. After working as an assistant professor at Muroran Institute of Technology, Japan, he was a postdoctoral researcher at Pattern Recognition Group, University of Siegen, Germany, from 2013 to 2018. He was then an associate professor at Kindai University, Japan from 2018 to 2023. Afterward, he started to work as an associate professor at Doshisha University, Japan and is currently a professor there. His research interests include multimedia data processing, machine learning, data mining, and sensor-based human activity recognition. He is a member of IEEE, ACM SIGKDD, ACM SIGMM, the Institute of Image Information and Television Engineers in Japan (ITE), the Information Processing Society of Japan (IPSJ), and the Institute of Electronics, Information and Communication Engineering in Japan (IEICE).

**Miki Yanobu** Miki Yanobu received her B.E. degree in engineering from Doshisha University, Japan, in 2025. Her bachelor thesis presented preliminary results of the decoder introduced in this paper.

**Kaduki Yamashita** Kaduki Yamashita is currently pursuing his B.E. degree at Doshisha University, Japan. His research interests include computer vision, with a particular focus on image generation using diffusion model.

**Miho Ohsaki** Miho Ohsaki received the B.E., M.E., and Dr. Eng. degrees from Kyushu Institute of Design (now, Kyushu University) in 1994, 1996, and 1999, respectively. From 1999 to 2004, she was an assistant professor at Shizuoka University. In 2004, she started working with Doshisha University, where she is currently a Professor. Her research interests include machine learning, knowledge discovery, and their application to biomedical data analysis. She is a member of IEEE, ACM, IEICE, IPSJ, JSAI, SOFT, and JAMI.